

Flanders
State of
the Art

18_044_1
FH Reports

FWO Nautical bottom

Comparison of numerical and experimental results
for the hydrofoil case tested in water

DEPARTMENT
**MOBILITY &
PUBLIC
WORKS**

www.flandershydraulics.be

FWO Nautical bottom

Comparison of numerical and experimental results for the hydrofoil case tested in water

Van Hoydonck, W.; Sotelo Zorrilla, M.; Lopez Castano, S.

Legal notice

Flanders Hydraulics is of the opinion that the information and positions in this report are substantiated by the available data and knowledge at the time of writing.

The positions taken in this report are those of Flanders Hydraulics and do not reflect necessarily the opinion of the Government of Flanders or any of its institutions.

Flanders Hydraulics nor any person or company acting on behalf of Flanders Hydraulics is responsible for any loss or damage arising from the use of the information in this report.

Copyright and citation

© The Government of Flanders, Department of Mobility and Public Works, Flanders Hydraulics, 2025

D/2025/3241/139

This publication should be cited as follows:

Van Hoydonck, W.; Sotelo Zorrilla, M.; Lopez Castano, S. (2025). FWO Nautical bottom: Comparison of numerical and experimental results for the hydrofoil case tested in water. Version 2.0. FH Reports, 18_044_1. Flanders Hydraulics: Antwerp

Reproduction of and reference to this publication is authorised provided the source is acknowledged correctly.

Document identification



Customer:	Flanders Hydraulics	Ref.:	WL2025R18_044_1
Keywords (3-5):	surface-piercing rudder, CFD, EFD		
Knowledge domains:	Harbours and waterways > Manoeuvring behaviour > Nautical bottom > Scale model tests		
Text (p.):	27	Appendices (p.):	0
Confidential:	No	<input checked="" type="checkbox"/> Available online	

Author(s):	Van Hoydonck, W.; Sotelo Zorrilla, M.
------------	---------------------------------------

Control

	Name	Signature
Revisor(s):	Lopez Castano, S.	Getekend door:Santiago LOPEZ CASTA Getekend op:2025-06-23 14:27:34 +02:0 Reden:Ik keur dit document goed  
Project leader:	Van Hoydonck, W.	Getekend door:Wim Van Hoydonck (Sign Getekend op:2025-06-16 16:11:38 +02:0 Reden:Ik keur dit document goed  

Approval

Head of division:	Bellafkih, A.	Getekend door:Abdelkarim Bellafkih (Sig Getekend op:2025-06-16 21:52:31 +02:0 Reden:Ik keur dit document goed  
-------------------	---------------	---

Abstract

In the Fonds Wetenschappelijk Onderzoek (FWO) nautical bottom project, experiments have been executed with two objects in the inclined channel at Flanders Hydraulics (FH). The purpose of the experiments was to obtain validation data for the Computational Fluid Dynamics (CFD) model that has been developed at KULeuven. In the first test campaign, a cylinder was used and in the second one, a surface-penetrating rudder was tested. For both cases, tests were first executed where the tank was filled with water alone. Afterwards, tests are executed with mud and a combination of water and mud at different under-keel clearances. In the current report, the experimental results obtained with the rudder setup in water are compared with CFD results obtained with FINE/Marine. The focus is on the lift and drag forces generated by the rudder in addition to the yawing moment. In the experiments, the rudder is tested at multiple incidence angles between -10° and 10° . The computations focus on a single incidence angle of -10° for speeds in the range $V = 0.2 \text{ m/s}$ to $V = 1.2 \text{ m/s}$. Due to the relatively low Reynolds numbers (which places the tests in the middle of the transition from laminar to turbulent flow), the influence of the turbulence closure model is tested as well: computations are executed using pure laminar flow and fully turbulent flow. In addition, some computations are executed with the simplified one-parameter transition model available in FINE/Marine. All computations are executed assuming steady flow conditions. Apart from the force comparison, pressure measured on the rudder is compared to the pressure field obtained in CFD. The trends for the forces and pressure values as a function of tow speed as measured in the experiments are captured in the numerical results, although some differences remain. The one-parameter transition model is used without tuning and generates results that are situated between the fully laminar and fully turbulent results. The point pressure measurements on the rudder surface (in addition to the total forces and moments) are valuable for validation purposes. Overall, the correspondence between experimental and numerical results is encouraging, but differences remain. The case itself is however fairly complex, as at low speeds, both the turbulence model and time integration scheme influence the results, while at high speeds, the high Froude numbers (and associated significant water surface deformations) can be challenging for two-phase solvers as well.

Contents

Abstract	III
List of Figures	V
List of Tables	VI
Nomenclature	VII
1 Introduction	1
2 Experimental setup	2
2.1 Facility	2
2.2 Geometry	3
2.3 Experimental condition	5
2.4 Signal post-processing	5
2.4.1 Determination of the steady time period	6
2.4.2 Spectrogram of the signal	7
2.4.3 FFT of the signal	8
2.4.4 Calculation of the uncertainty using the RUM method	8
2.5 Force measurements	9
2.6 Pressure measurements	11
3 Numerical setup	13
3.1 Introduction	13
3.2 Domain geometry and grid generation	13
3.3 Solver settings	14
3.4 Dimensionless quantities	14
4 Results	15
4.1 Flow visualisations	15
4.2 Convergence of integral quantities	17
4.3 Comparison with experimental results	19
4.3.1 Forces	19
4.3.2 Pressure measurements	21
5 Conclusions	25
6 Acknowledgements	26
References	27

List of Figures

Figure 1	Side view of the inclined channel at FH. The internal section measures $0.56 \text{ m} \times 0.76 \text{ m}$	2
Figure 2	Installation drawing of the rudder with load cell in the inclined channel.....	2
Figure 3	Model 6A40 load cell from Interface, Inc.	3
Figure 4	Installation of the rudder in the inclined channel with three pressure holes visible on the port side.	3
Figure 5	Locations of the four rudder probes.	4
Figure 6	Comparison of the scanned rudder geometry with the 3D model.	4
Figure 7	Scanned rudder geometry, holes filled and trailing edge reconstructed suitable for CFD computations.	5
Figure 8	Velocity profile for the test at $V = 1.2 \text{ m/s}$	6
Figure 9	Raw signal of longitudinal force X at $V = 1.2 \text{ m/s}$. The moving average of the signal is shown in orange.	7
Figure 10	Spectrogram of the longitudinal force X for $V = 1.2 \text{ m/s}$	7
Figure 11	Power Spectral Density (PSD) of the longitudinal force X for $V = 1.2 \text{ m/s}$	8
Figure 12	Part of longitudinal force X in the period with steady velocity for $V = 1.2 \text{ m/s}$	9
Figure 13	Average and uncertainty of the filtered longitudinal force signal X at a velocity $V = 1.2 \text{ m/s}$. .	9
Figure 14	Forces (left) and moments (right) acting on the rudder as a function of tow speed in freshwater for different incidence angles.	10
Figure 15	Rudder coefficients as a function of tow speed in freshwater for different incidence angles.	11
Figure 16	Hydrodynamic pressure values as a function of tow speed for the rudder for $\beta = 10^\circ$	12
Figure 17	Grid slices through the rudder at $x = 0 \text{ m}$ (left) and $z = -0.05 \text{ m}$ (right).....	13
Figure 18	Wave elevation around the rudder at $V = 1.0 \text{ m/s}$ and $\beta = 10^\circ$	15
Figure 19	Hydrodynamic pressure and velocity magnitude in the horizontal plane at $z = -0.05 \text{ m}$ for the rudder at $V = 1.0 \text{ m/s}$ and $\beta = 10^\circ$	16
Figure 20	Comparison of velocity field at $z = -0.05 \text{ m}$ for fully turbulent (left) and fully laminar (right) flow assumptions for $V = 0.5 \text{ m/s}$	16
Figure 21	Comparison of velocity field at $z = -0.05 \text{ m}$ for fully turbulent (left) and fully laminar (right) flow assumptions for $V = 0.2 \text{ m/s}$	16
Figure 22	Convergence of forces and moments acting on the rudder for $V = 1.0 \text{ m/s}$ and $\beta = 10^\circ$ assuming fully turbulent flow.	17
Figure 23	Convergence of the forces and moments acting on the rudder at $V = 0.5 \text{ m/s}$ and $\beta = 10^\circ$ assuming fully turbulent flow.	18
Figure 24	Convergence of the forces and moments acting on the rudder at $V = 0.5 \text{ m/s}$ and $\beta = 10^\circ$ assuming laminar flow.	18
Figure 25	Convergence of the forces and moments acting on the rudder at $V = 0.5 \text{ m/s}$ and $\beta = 10^\circ$ assuming free transition from laminar to turbulent flow.	19
Figure 26	Comparison of experimental and numerical values of lift, drag and yawing moment coefficients for drift angle $\beta = 10^\circ$	20
Figure 27	Comparison of experimental and numerical values of lift, drag and yawing moment coefficients for drift angle $\beta = 10^\circ$	21
Figure 28	Comparison of velocity field at $z = -0.05 \text{ m}$ for steady (top) and unsteady (bottom) turbulent flow assumption for drift angle $\beta = 10^\circ$ and $V = 0.2 \text{ m/s}$	21
Figure 29	Comparison of the pressure distribution on the rudder for the laminar and turbulent case at $V = 0.4 \text{ m/s}$ and $\beta = 10^\circ$	22
Figure 30	Comparison of the pressure distribution in the plane $z = -0.05 \text{ m}$ for the laminar and turbulent case at $V = 0.4 \text{ m/s}$ and $\beta = 10^\circ$	23
Figure 31	Comparison of numerical and experimental hydrodynamic pressure values at the rudder probes.	24

List of Tables

Table 2	X- and y-coordinates of the centres of the probes on the surface of the rudder profile.	4
Table 3	Reynolds number Re and Froude number Fr as a function of the tow velocity for a water temperature of 15 °C.	6

Nomenclature

Abbreviations

CFD	Computational Fluid Dynamics
EFD	Experimental Fluid Dynamics
FFT	Fast Fourier Transform
FH	Flanders Hydraulics
FWO	Fonds Wetenschappelijk Onderzoek
PSD	Power Spectral Density

1 Introduction

The objective of the experiments for the FWO nautical bottom project is to generate validation data for an OpenFOAM CFD model developed at KULeuven to predict by numerical means the behaviour of a ship sailing in or above a layer of mud. In this report, a comparison is made between experimental data obtained in the inclined channel at FH using a symmetrical surface-piercing rudder submerged 0.15 m in water with a drift angle $\beta = 10^\circ$ for a range of velocities, and numerical results computed with FINE/Marine for the same conditions. In part, the research reported here has been presented at the 35th Symposium on Naval Hydrodynamics (Sotelo *et al.*, 2024). The bulk of the research within this FWO project has been carried out by Marco Sotulo (Ghent University) and Praveen Doddugollu (KU Leuven), whose doctoral dissertations contain all details on the experimental research (Sotelo, 2024) and the numerical model development (Doddugollu, 2024).

2 Experimental setup

2.1 Facility

The experiments are executed in the inclined channel at FH, which has a length of 20 m, a width of 0.56 m and a depth of 0.76 m (Fig. 1). The setup consists of a surface piercing rudder (NACA 0015) that is submerged 0.15 m in still water. The incidence angle of the rudder can be chosen in the range -10° to 10° in steps of 2.5° . The rudder is accelerated to a desired tow speed and all three force and moment components on the rudder are measured using a six axis load cell attached to the carriage above the rudder. Initially, the plan was to submerge the rudder 20 cm into the water (as shown in Fig. 2), but the initial tests revealed that water from the bow wave flowed over the top of the rudder at high speeds. For this reason, the draft was reduced by 5 cm to 15 cm.

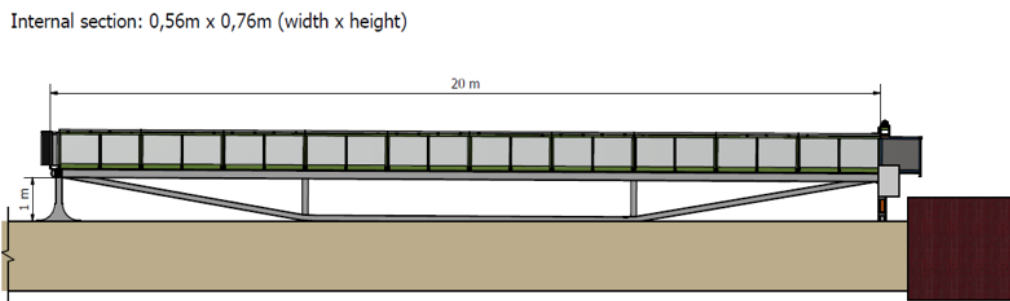


Figure 1 – Side view of the inclined channel at FH. The internal section measures 0.56 m \times 0.76 m.

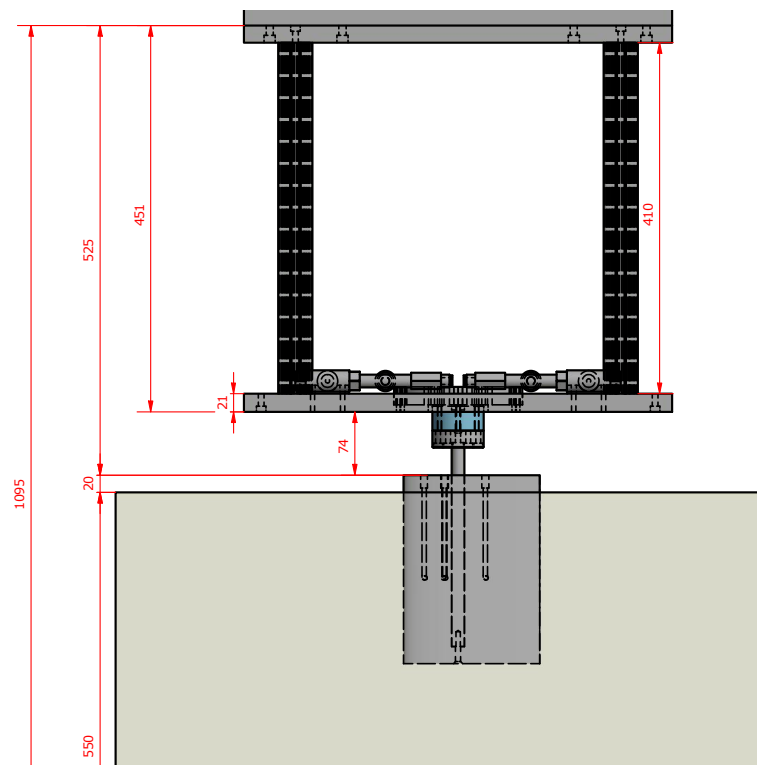


Figure 2 – Installation drawing of the rudder with load cell in the inclined channel.

2.2 Geometry

The rudder has been 3D-printed at Materialise¹ with the Selective Laser Sintering (SLS) technique. The tolerances for SLS technology is $\pm 0.3\%$. The load cell (Model 6A40, shown in Fig. 3) is manufactured by Interface². In addition to the load cell, four pressure sensors are installed that measure the pressure at the rudder surface at four points located in the same horizontal plane 0.05 m below the free surface. Three probes are located on one side (visible in Fig. 4) and the fourth is located in the opposite side. A graph with the locations of the probes on the rudder profile are shown in Fig. 5 and the coordinate values of each of the probe locations are listed in Table 2. Additionally, two sets of four pressure probes are installed along the flume at 5 and 10 m from the starting point. The signals coming from these pressure probes are also recorded, however, post-processing is different from the previously mentioned signals.



Figure 3 – Model 6A40 load cell from Interface, Inc.

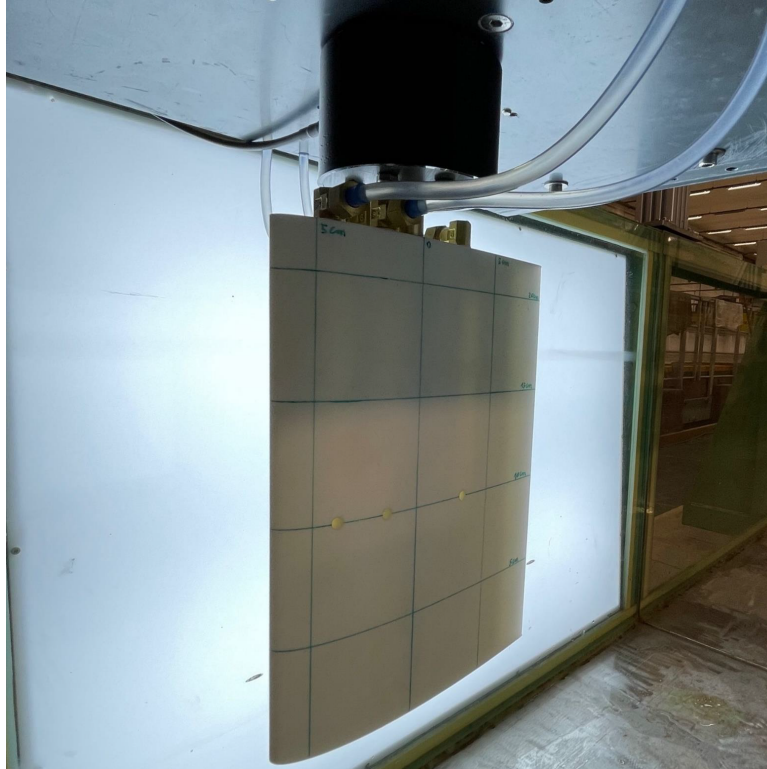


Figure 4 – Installation of the rudder in the inclined channel with three pressure holes visible on the port side.

¹<https://www.materialise.com>

²<https://www.interfaceforce.com>

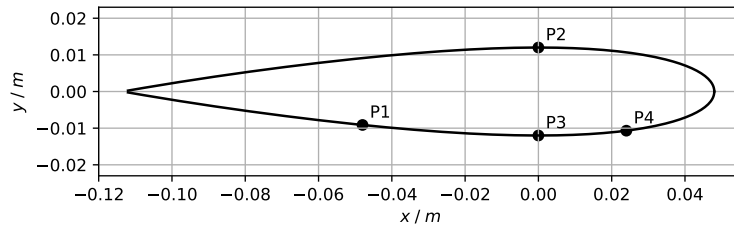


Figure 5 – Locations of the four rudder probes.

Table 2 – X- and y-coordinates of the centres of the probes on the surface of the rudder profile.

probe	x	y
P1	-4.800×10^{-2}	-9.127×10^{-3}
P2	0.0	1.200×10^{-2}
P3	0.0	-1.200×10^{-2}
P4	2.400×10^{-2}	-1.069×10^{-2}

After finishing the experimental program with the rudder (and the CFD computations), the geometry of the rudder was 3D scanned. A comparison of the scanned geometry with the original 3D model is shown in Fig. 6. The opposite colours on either side indicate a slight bend of the vertical profile of the hydrofoil geometry: yellow colours indicate an outward bulge of the printed shape as compared to the 3D model, blue colours indicate an inward bulge of the shape. As a result, this gives the rudder a slight camber: at zero degrees angle of attack, the rudder will not generate zero lift and the pitching moment may be non-zero.

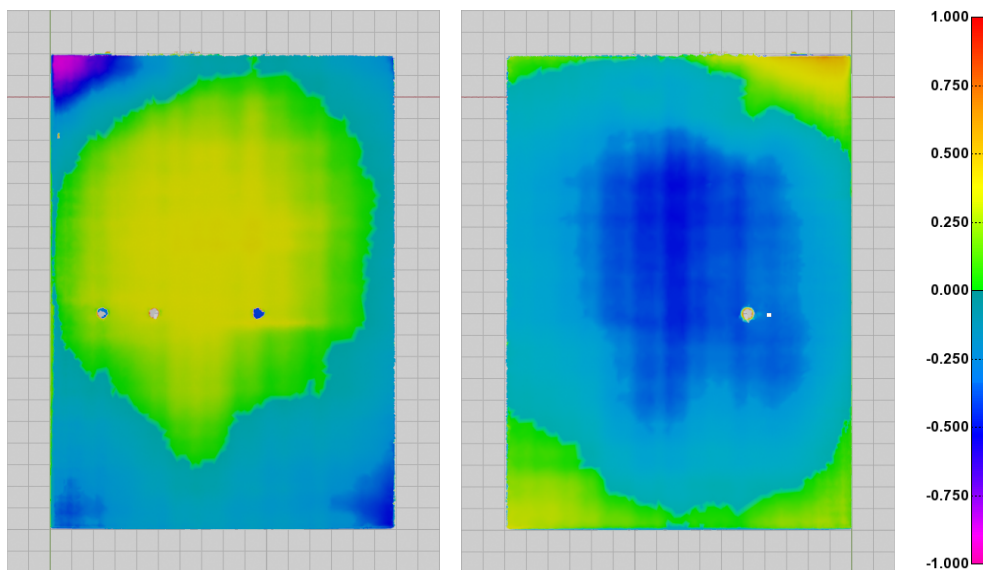


Figure 6 – Comparison of the scanned rudder geometry with the 3D model, left: port side, right: starboard side. Units are in mm, yellow colours indicate an outward bulge of the printed shape as compared to the 3D model, blue colours indicate an inward bulge of the 3D printed shape. The opposite colours on either side indicate a slight bend of the vertical profile of the hydrofoil geometry.

The scanned rudder geometry misses the largest part of the top surface and the trailing edge. To use the scanned geometry for CFD computations, the holes were filled with a discretisation of the theoretical hull geometry. The locations of the pressure probes were filled in as well. The resulting geometry (shown in Fig. 7) was placed inside a domain box and together, these were triangulated and exported as a coloured STL for use in HEXPRESS³.

³HEXPRESS cannot combine STL geometry and parametric (solid) geometry to construct a domain.

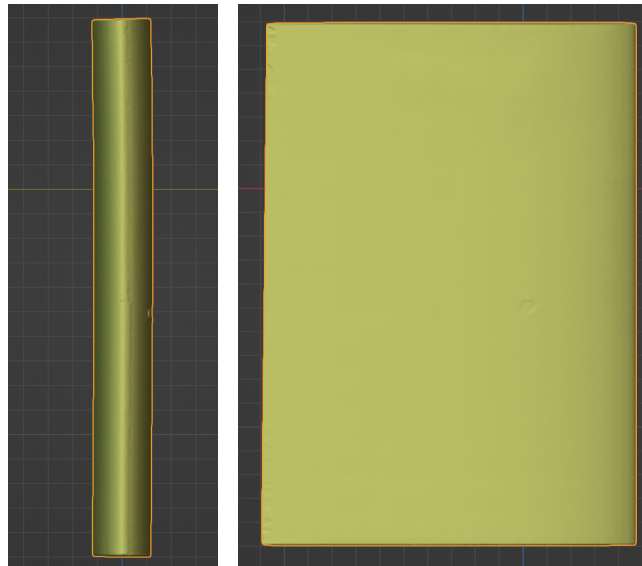


Figure 7 – Scanned rudder geometry, holes filled and trailing edge reconstructed suitable for CFD computations. The front view (left) shows the bend in the profile, the side view (right) shows that the trailing edge is not perfectly vertical.

The 3D scan of the rudder geometry results in rounded edges between the side surface and top and bottom surfaces. This may reduce the strength of longitudinal vortices at locations where flow separation occurs. The front view in Fig. 7 shows the curvature in the profile. What is also visible is that both the top and bottom faces are not parallel, but slightly tilted. This may suggest that the process of 3d printing the geometry resulted in internal stresses that were released afterwards. It is not clear if the hole through the rudder contains the same curvature.

2.3 Experimental condition

For the current investigation, tests are executed with the channel filled with water alone. These tests serve as validation cases for the experimental setup before more complex cases with mud alone or a mud and water are tackled.

The Reynolds number based on the rudder chord length c and the maximum and minimum velocities of $V_{max} = 1.2$ m/s and $V_{min} = 0.1$ m/s equal $Re_{max} = 168\,500$ and $Re_{min} = 14\,000$ for a water temperature of 15 °C. The rudder pierces the water surface, so the Froude number is an important quantity as well: it varies from $Fr = 0.08$ for $V = 0.1$ m/s to $Fr = 0.96$ for $V = 1.2$ m/s. Reynolds and Froude numbers for the tow velocities as used in the experiments are listed in Table 3. Experimental flow conditions where the Reynolds number is between 10 000 and 150 000, can be considered to be in the transition zone from laminar to turbulent flow (Van Hoydonck *et al.*, 2017). Only for the highest velocities, one can assume fully turbulent flow.

2.4 Signal post-processing

All signals coming from the instrumentation of the experimental setup are post-processed using filters and numerical techniques implemented in Python. The post-processing steps for the signals coming from load cell and the pressure sensors on the rudder are elaborated here.

Table 3 – Reynolds number Re and Froude number Fr as a function of the tow velocity for a water temperature of 15 °C.

$V / m/s$	Re	Fr
0.1	1.4047×10^4	0.0798
0.2	3.0613×10^4	0.159
0.3	4.5927×10^4	0.239
0.4	6.1227×10^4	0.319
0.5	7.6534×10^4	0.400
0.6	9.1840×10^4	0.479
0.7	1.0715×10^5	0.559
0.8	1.2245×10^5	0.636
0.9	1.3776×10^5	0.718
1.0	1.5307×10^5	0.798
1.1	1.6837×10^5	0.878
1.2	1.8368×10^5	0.958

2.4.1 Determination of the steady time period

The first step in the post-processing procedure is to find the steady time period of the tests. For each test the reference velocity is defined manually. Using the velocity signal coming from the PLC it is easy to find the section of the tests which corresponds to the steady velocity. To avoid potential interference in the analysis, only a portion of this steady section is used. Once the complete steady section is determined, the first 20% of the signal corresponding to the initial acceleration is discarded. At the end of the steady section, the last 20% before the deceleration starts, is also discarded, the remaining section in between these two time instances is assumed steady and used for post-processing. In Fig. 8 the section of the signal used in the post-processing phase is highlighted in green.

Most of the signals from the different instrumentation used in the experimental setup have an initial offset. The zero section or initial condition of the signal is determined when the PLC velocity result is oscillating around 0 (the carriage is not moving). Once the end of the initial section is found, only 75% of the zero region is used to calculate the initial conditions. In Fig. 8 can be noticed the section of the test based on the PLC results. The final value of each measurement is the result of subtracting the initial condition from average value of the steady section.

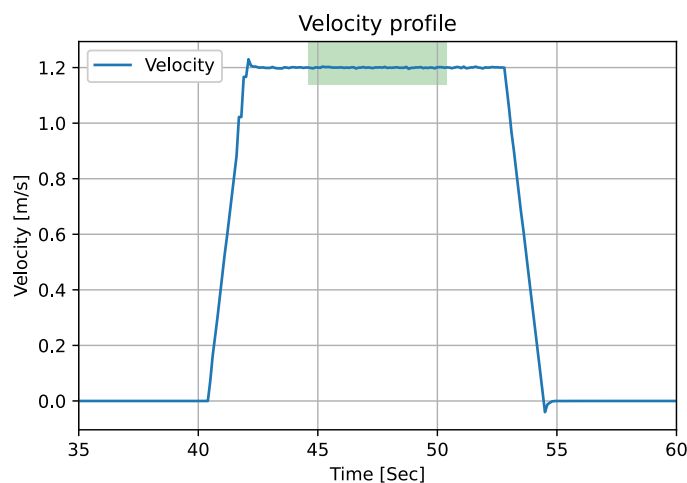


Figure 8 – Velocity profile for the test at $V = 1.2$ m/s.

An example of the raw signal coming from the load cell is presented in Fig. 9, where the raw X-force for a test executed at $V = 1.2$ m/s is shown.

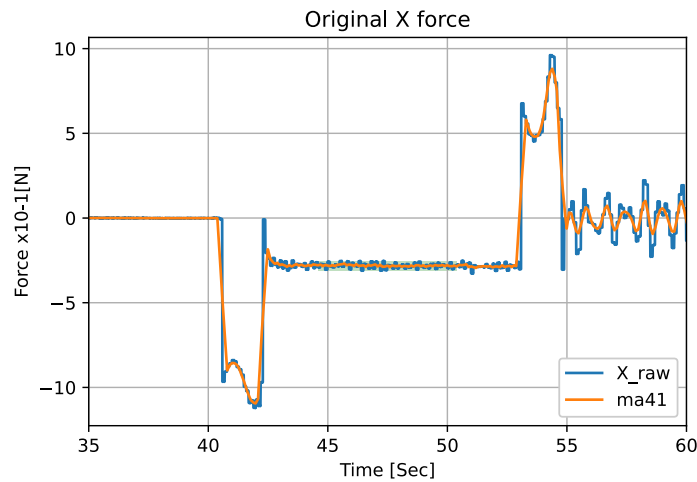


Figure 9 – Raw signal of longitudinal force X at $V = 1.2$ m/s. The moving average of the signal is shown in orange.

2.4.2 Spectrogram of the signal

One way to evaluate the type of signal obtained from the sensors is to compute a spectrogram of the raw output. The spectrogram is a signal processing tool that can be used to visualize the frequency spectrum of a signal as it varies in time. Similar to the Fast Fourier Transform (FFT), the advantage of using a spectrogram is its capability to check when the dominant frequencies are present at the different stages of the test. The physical phenomena during each tests are expecting to be present in the low frequency range (below 10 Hz). In steady tests, it is interesting to check whether the dominant frequencies related to the physical phenomena are constant during the test. Also the spectrogram helps in the identification of different frequencies that are intrinsic to the system e.g. carriage vibrations, etc. In Fig. 10 the spectrogram of the raw force signal in the longitudinal direction (displayed before in Fig. 9) is presented.

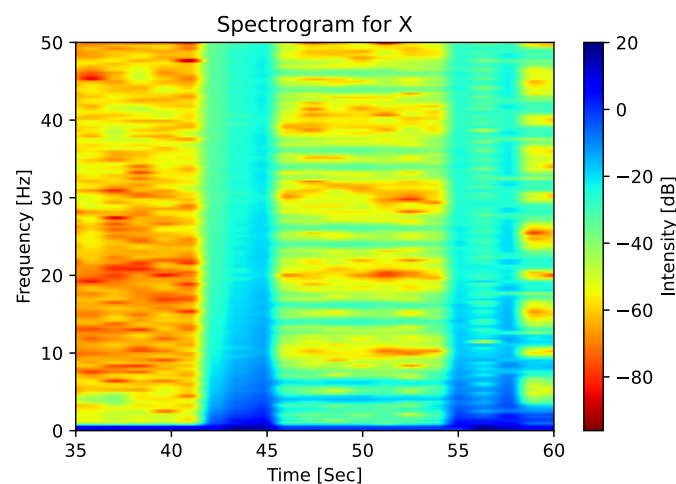


Figure 10 – Spectrogram of the longitudinal force X for $V = 1.2$ m/s.

Inspection of this figure and Fig. 8 (where the velocity ramp of the same test is presented), one can conclude that the steady velocity section of the test starts at about 42 seconds. In the spectrogram one can also notice a

change in the behaviour of the spectrum after 42 seconds. The dominant components of the signal have a very low frequency (between 0 to 1 Hz) which correspond to the actual force recorded. Furthermore, low intensity signals with higher frequencies appear once the steady section of the test is reached. The latter frequencies can be related to intrinsic noise of the system or the sensors itself, but these remain constant during the test which is expected in the steady section of the experiment. By using the spectrogram it is possible to realize that the frequency of the noise presented in the signal is outside of the range of interest. Then it is safe to assume that from the raw signal recorded, all the components of the spectrum bellow 10 Hz can be used as a filtered signal. The rest will be considered as noise. This analysis is repeated for all the load cells and pressure sensors used in the experimental setup.

2.4.3 FFT of the signal

Once the steady section of the signal is determined, the subsequent step is to decompose the signal in the frequency domain using the FFT. From the PSD distribution it is possible to eliminate from the raw signal the white noise or any other high frequency noise that affects the measurement. Based on the analysis of the spectrogram of the signal a 10 Hz threshold was used to remove the noise. In the following example the raw signal of X in the selected region of the steady velocity is used to compute the FFT. By removing the part of the signal considered as noise (above 10 Hz) and computing the inverse Fourier transform, the filtered signal is presented in Fig. 12.

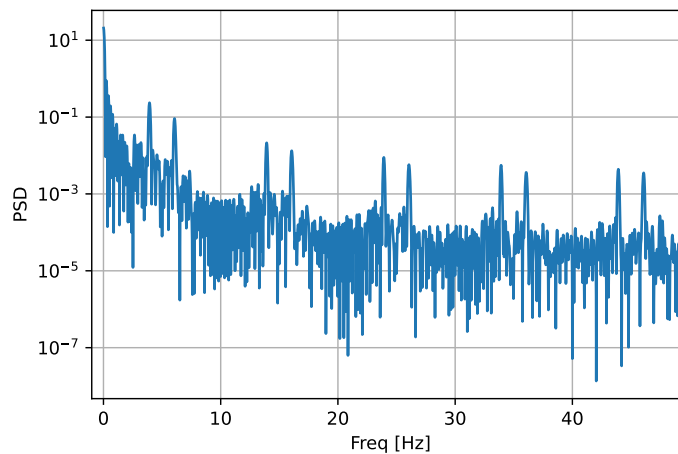


Figure 11 – PSD of the longitudinal force X for $V = 1.2$ m/s.

After the low bandwidth filtering technique is applied, it is possible to have a better idea of the actual value in which the signal is oscillating, hence having a more precise value of the average. The same filtering process is used in the output signal of the load cell and pressure sensors located in the hydrofoil.

2.4.4 Calculation of the uncertainty using the RUM method

The method to estimate the uncertainty of the measurements is the Random Uncertainty of the Mean (RUM) proposed by Brouwer *et al.* (2019). This method is based on the auto-covariance of the random signal and is specifically designed for stationary signals. This numerical technique is used to estimate an uncertainty with 95% of confidence for a single stationary signal, without the necessity to conduct a significant number of repetitions. More information about the method can be found in Brouwer *et al.* (2019). To study the behaviour of the average and its uncertainty, Brouwer *et al.* recommends to follow a lag method, which consist of taking

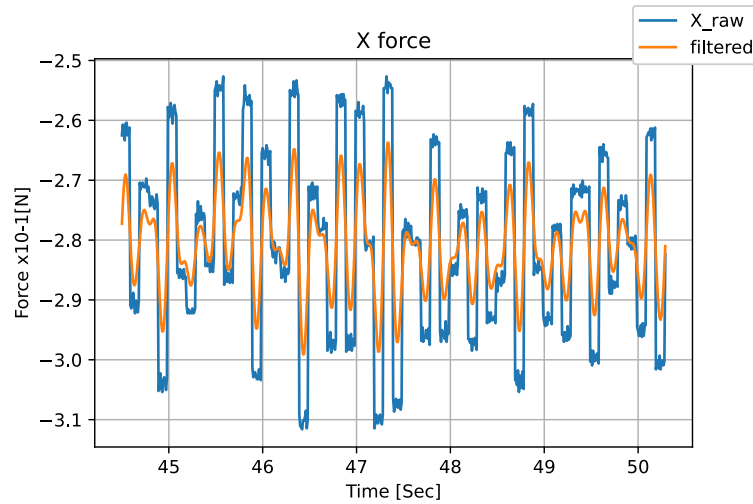


Figure 12 – Part of longitudinal force X in the period with steady velocity for $V = 1.2$ m/s.

portions of the signal and calculating the cumulative average and uncertainty. For example the first portion or lag for the calculation could be 10 % of the total signal, the second could be 15% and gradually increase the sampling size until the complete signal is included in the computation. As such, it is possible to notice any instability or unsteadiness in the recorded signal. In Fig. 13, the implementation of the RUM method is illustrated for the longitudinal force X . One can observe that the average value converges as the sampling size increases. This behaviour is expected for the mean value of a stationary signal, because as the size of the sample is increased, the mean tends to the expected value. Something similar can be observed for the uncertainty value (Fig. 13b), it tends to the final value as the sampling size increases. This procedure is performed after the filtering of the signal and is repeated for all the signals coming from the load cell and pressure sensors in the body.

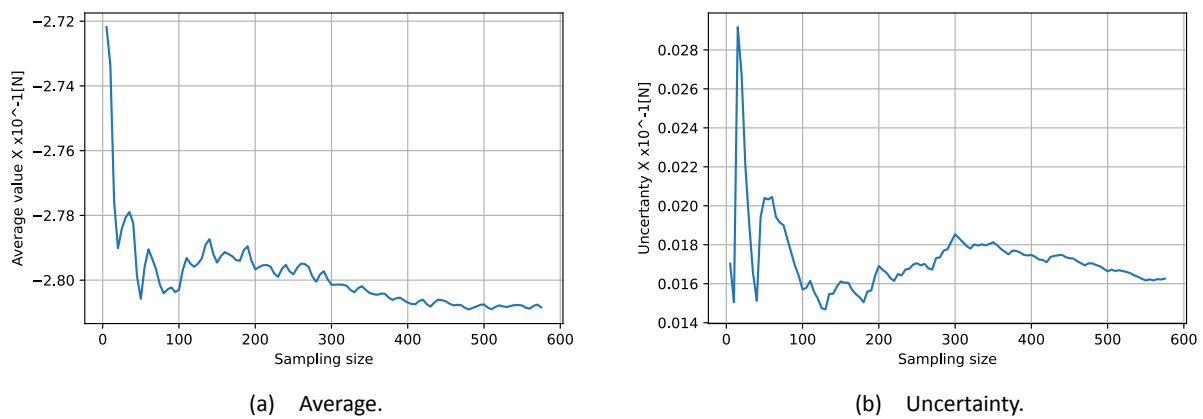


Figure 13 – Average and uncertainty of the filtered longitudinal force signal X at a velocity $V = 1.2$ m/s.

2.5 Force measurements

The post-processing techniques explained before were used to process the hydrodynamic forces acting on the rudder during tow tests in fresh water. The dimensional force components (resolved in the axes system aligned with the inclined channel) as a function of the tow speed are presented in Fig. 14. The equivalent coefficients

are shown in Fig. 15, which are not shown for velocities lower than $V = 0.2$ m/s. There are distinct differences in the trends below and above $V = 0.8$ m/s, these are caused by the changing physics as both the Froude number and Reynolds number change.

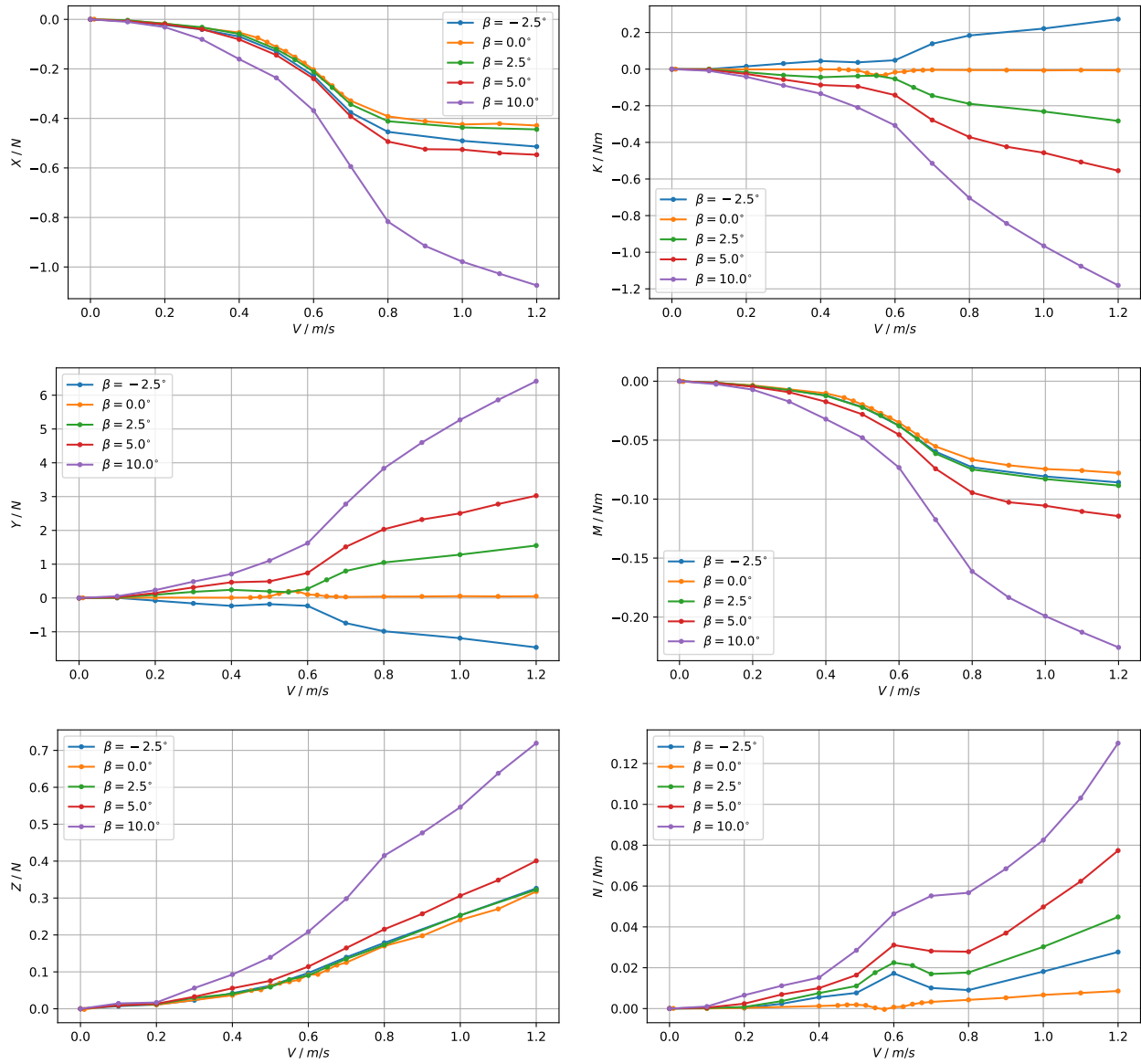


Figure 14 – Forces (left) and moments (right) acting on the rudder as a function of tow speed in freshwater for different incidence angles.

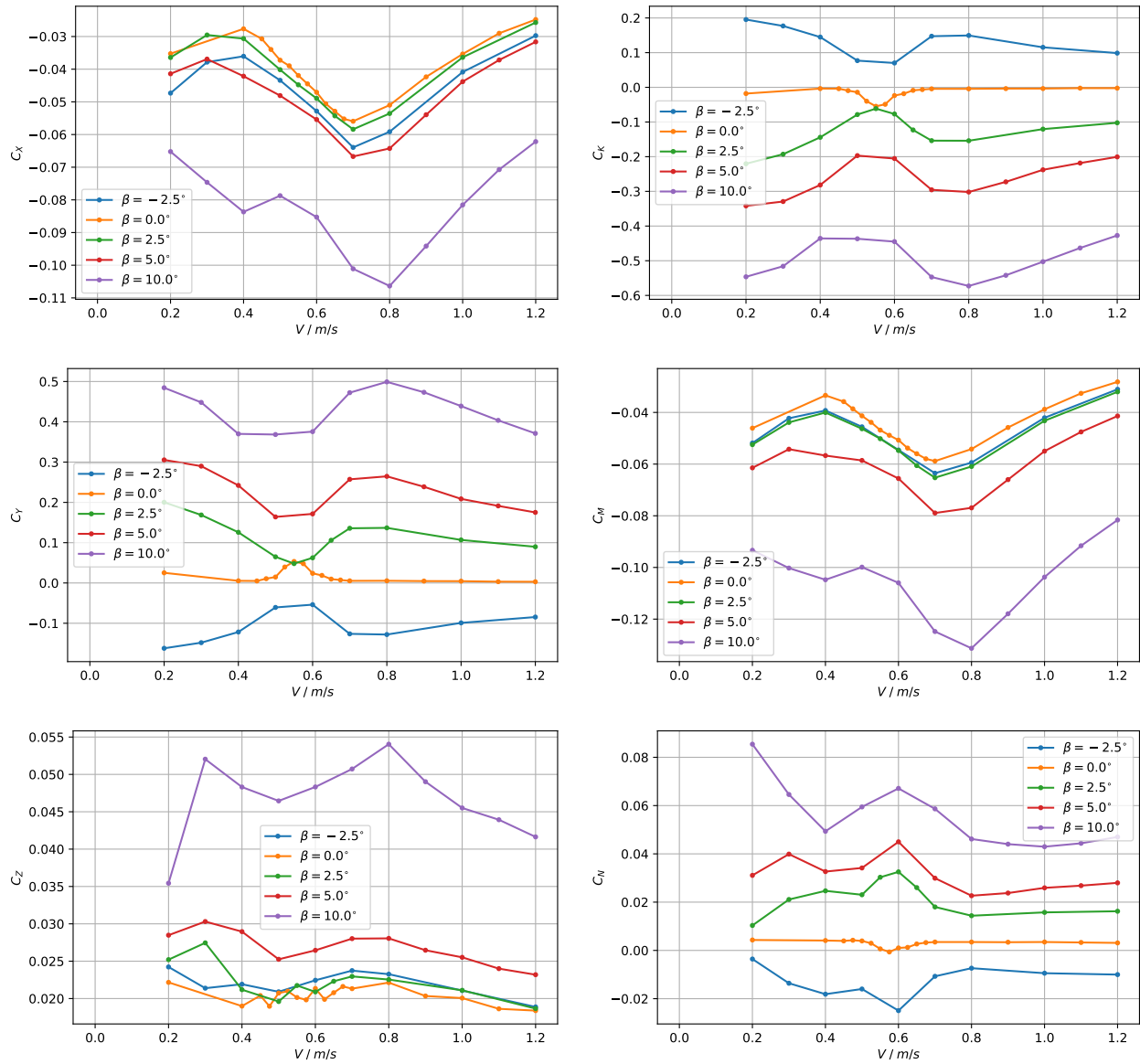


Figure 15 – Rudder coefficients as a function of tow speed in freshwater for different incidence angles.

2.6 Pressure measurements

As stated before, pressure measurements were recorded at four points on the surface of the rudder in a plane 5 cm below the free surface (or 10 cm from the rudder bottom). Before the start of each experimental run, static pressure values are recorded and those are subtracted from the values measured during the run. The offset that is subtracted corresponds to the hydrostatic pressure,

$$\Delta p = \rho g z \approx 1000 \cdot 9.81 \cdot 0.05 = 490.5 \text{ Pa.} \quad (1)$$

The resulting values can be directly compared with the hydrodynamic pressure values output by the CFD solver. The measured hydrodynamic pressure values as a function of the tow speed for the rudder at an incidence angle of 10° are shown in the Fig. 16. Uncertainties computed with the method described in ¶ 2.4.4 are shown in this figure as a semi-transparent band behind the average values. On the pressure side (P4), a globally linear trend is observed (with some deviation from the linear trend near $V = 0.7 \text{ m/s}$). On the suction side, significant changes occur in the measured pressure values as the velocity is increased, with trends that are far from linear.

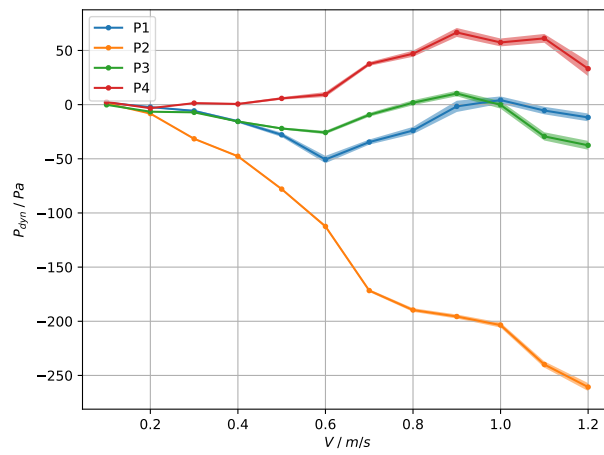


Figure 16 – Hydrodynamic pressure values as a function of tow speed for the rudder for $\beta = 10^\circ$.

3 Numerical setup

3.1 Introduction

Numerical computations are executed with FINE/Marine version 12.1 with a setup that includes the free water surface. Since the range of velocities ($V = 0.1 \text{ m/s}$ to 1.2 m/s) corresponds to a Reynolds number range of $Re = 14\,000$ to $168\,500$, this places the experiments in the middle of transition from laminar to turbulent flow. The main purpose of these computations is to compare the numerical results with the experimental measurements, where the influence of the turbulence model choice is assessed. Apart from assuming fully laminar or turbulent flow, FINE/Marine includes transition models as well.

The rudder pierces the water surface, which makes the Froude number an important quantity as well: it varies from $Fr = 0.08$ to $Fr = 0.96$ for the velocity range of the experiments.

3.2 Domain geometry and grid generation

The domain has a length of 4 m, a height of 1 m and the width corresponds to the width of the experimental facility (0.56 m).

A single grid is generated for a single incidence angle of $\beta = 10^\circ$. For the viscous layers around the rudder, the turbulent flow conditions are used to determine the thickness of the first cell size in the boundary layer. Using a reference speed of $V = 1 \text{ m/s}$, freshwater fluid properties and a target Y^+ of 0.8, the first layer thickness equals $2.139\,666 \times 10^{-5} \text{ m}$. The interface between water and air is captured with a refinement surface with a large diffusion factor and a vertical resolution of approximately 0.001 m. After inserting viscous layers, the grid contains approximately 4.686×10^6 cells.

Cross sections of the grid near the rudder are shown in Fig. 17.

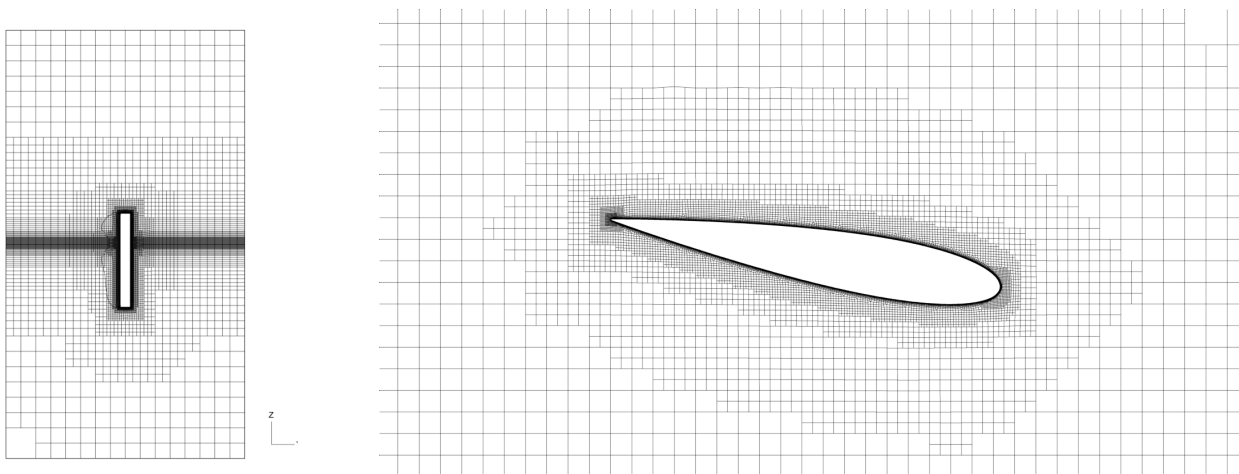


Figure 17 – Grid slices through the rudder at $x = 0 \text{ m}$ (left) and $z = -0.05 \text{ m}$ (right).

3.3 Solver settings

Due to the preliminary investigation of these computations, the solver settings are kept fairly straightforward. The two-phase nature of the problem requires a time stepping approach by the solver to obtain a converged solution. The time integration itself is first-order, this corresponds to the *steady* setting in the interface.

The density and dynamic viscosity of the water fraction are the same as measured in the experiments (998.4 kg/m³ and 0.00104362 Pa s). The air density is 1.2 kg/m³ and its dynamic viscosity equals 1.85×10^{-5} Pa s. The gravitational acceleration equals 9.81 m/s².

The two lateral sides and the bottom of the domain are treated as solid bodies with wall functions. At the top of the domain, the pressure is prescribed (*Updated hydrostatic pressure*). Both the inlet and outlet, the *far field* condition is prescribed with zero velocity.

Motion of an object in FINE/Marine is implemented by assigning a motion law to the object itself instead of adapting the boundary conditions. For this particular case, the surge motion is imposed. A ramp is imposed that smoothly increased the velocity of the rudder from zero to the desired final velocity. For all cases, acceleration period lasts for five seconds, after which the velocity is kept constant. All of the other degrees of freedom of the rudder are fixed. The reference point for the computation of forces and moments is set to the origin of the domain axes system, which coincides with the vertical location of the water surface, at the rotation axes of the rudder. By default, the time step depends on the reference length and reference speed of the object, and for VOF computations with no solved degrees of freedom, the time step follows from,

$$\Delta t = 0.01 \frac{L_{ref}}{V_{ref}}, \quad (2)$$

where the reference length L_{ref} equals the rudder chord (16 cm), and the reference velocity equals the desired velocity. For low-speed cases, experience has shown that the suggested time step is too large. For the current investigation, the time step is not increased beyond $\delta t = 0.003$ s.

All computations are run for at least 10 000 time steps. Inspection of the convergence trends of forces showed that this was enough for all of the computations except for the lowest velocities, for which the above number was doubled.

3.4 Dimensionless quantities

Forces and moments are non-dimensionalised using the following equations:

$$C_{X,Y,Z} = \frac{X,Y,Z}{\frac{1}{2}\rho V^2 S}, \quad (3)$$

$$C_{K,M,N} = \frac{K,M,N}{\frac{1}{2}\rho V^2 S c}, \quad (4)$$

where V is the reference speed, S is the surface area of the submerged rudder at zero speed (i.e $S = c \times T = 0.16 \text{ m} \times 0.15 \text{ m} = 0.024 \text{ m}^2$) and ρ is the water density.

4 Results

Results of all computations are discussed in this chapter. First some flow visualisations of the initial computation ($V = 1.0$ m/s) are shown. This is followed by a presentation of the convergence of integral quantities and a comparison with experimental results (integral forces and pressure values).

4.1 Flow visualisations

The deformation of the free surface is shown in Fig. 18. A significant depression in the water surface is visible on the suction side (bottom) of the rudder while at the pressure side (top) an increased water height is observed. The highest wave elevation is found at the leading edge of the rudder, near the stagnation point, where water is pushed up more than 4 cm above the still water level. This indeed confirms that in the original plan (with the rudder 0.2 m submerged), water would flow over the rudder top.

The hydrodynamic pressure and velocity magnitude around the rudder in the horizontal plane where the pressure probes are located are shown in Fig. 19. Hydrodynamic pressure values at the locations of the probes will be compared to experimental values in ¶ 4.3.2. In the cross section shown in Fig. 19, it is observed that the water flowing around the rudder remains attached at this angle of attack (as expected). The turbulent flow assumption combined with a relatively high Reynolds number (150×10^3) for this case is realistic, but may not hold true for (significantly) lower velocities. In Fig. 20, the relative velocity in the same horizontal plane is shown when the rudder moves at speed $V = 0.5$ m/s, for flow conditions assuming either fully turbulent and fully laminar flow. In this case, the turbulent flow remains attached over the complete rudder surface, while for the laminar flow condition, flow separation occurs near the trailing edge on the suction (bottom) side. As a laminar boundary layer is less energetic, it has more difficulty adhering to the rudder surface when encountering an adverse pressure gradient. For even lower velocities ($V = 0.2$ m/s), the flow field for laminar and turbulent flow conditions is shown in Fig. 21. This latter visualisation shows that at the lowest speeds tested, flow separation is practically inevitable. As speed is lowered, the assumption of using the first-order (steady) time integration in the solver is likely incorrect.

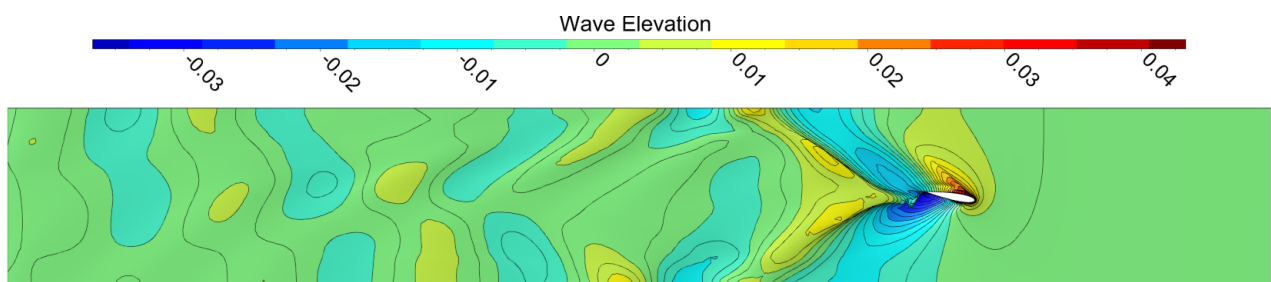


Figure 18 – Wave elevation around the rudder at $V = 1.0$ m/s and $\beta = 10^\circ$.

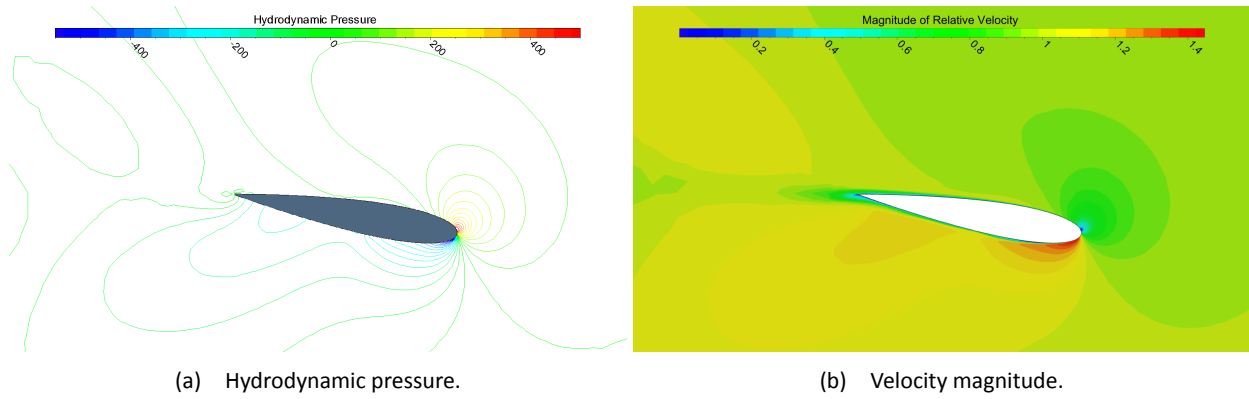


Figure 19 – Hydrodynamic pressure and velocity magnitude in the horizontal plane at $z = -0.05$ m for the rudder at $V = 1.0$ m/s and $\beta = 10^\circ$.

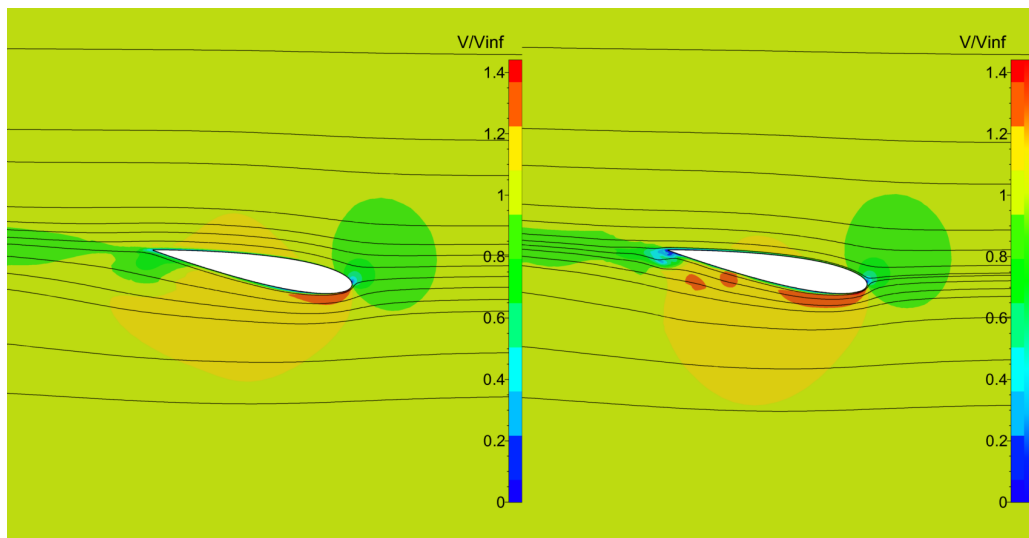


Figure 20 – Comparison of velocity field at $z = -0.05$ m for fully turbulent (left) and fully laminar (right) flow assumptions for $V = 0.5$ m.

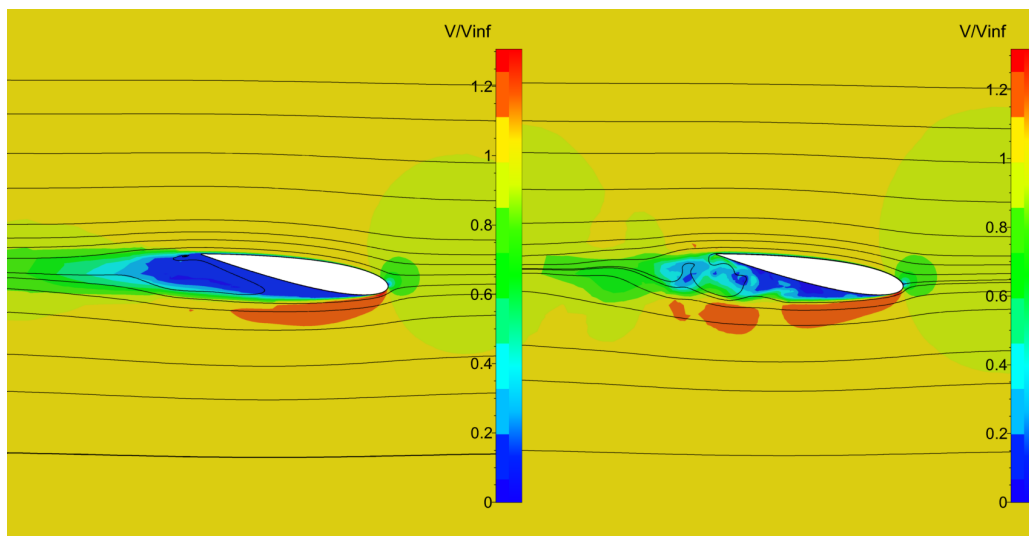


Figure 21 – Comparison of velocity field at $z = -0.05$ m for fully turbulent (left) and fully laminar (right) flow assumptions for $V = 0.2$ m.

4.2 Convergence of integral quantities

The convergence of the force components (F_x and F_y), and two moment components (M_x and M_z) are shown in Fig. 22. These graphs show the total value of the component (e.g. F_x), but also the pressure ($F_x P$) and viscous parts ($F_x V$) of said total value. Furthermore, the suffix *Dyn* denotes a correction of the quantity to exclude the hydrostatic pressure. The dashed lines visible in these graphs show the period used for averaging. For this velocity, using the last 4000 solver iterations for computing the averages is sufficient. With lower velocities convergence is slower, for example, Fig. 23 shows the convergence of the same force components for $V = 0.5$ m/s assuming fully turbulent flow. Similarly, the force convergence for the laminar case at this speed is shown in Fig. 24. Although this latter case also reaches a steady state, the magnitude of the fluctuations around the mean value are significantly higher. As discussed before, the laminar flow assumption results in a less energetic boundary layer that will detach earlier than a turbulent boundary layer. Lastly, Fig. 25 shows for the same condition, the convergence of the computation assuming transition from laminar to turbulent flow as available in FINE/Marine. Compared to either the fully turbulent and purely laminar cases, the convergence characteristics seem to be situated between the turbulent and laminar cases with more high-frequency fluctuations than turbulent case, but less than the laminar case.

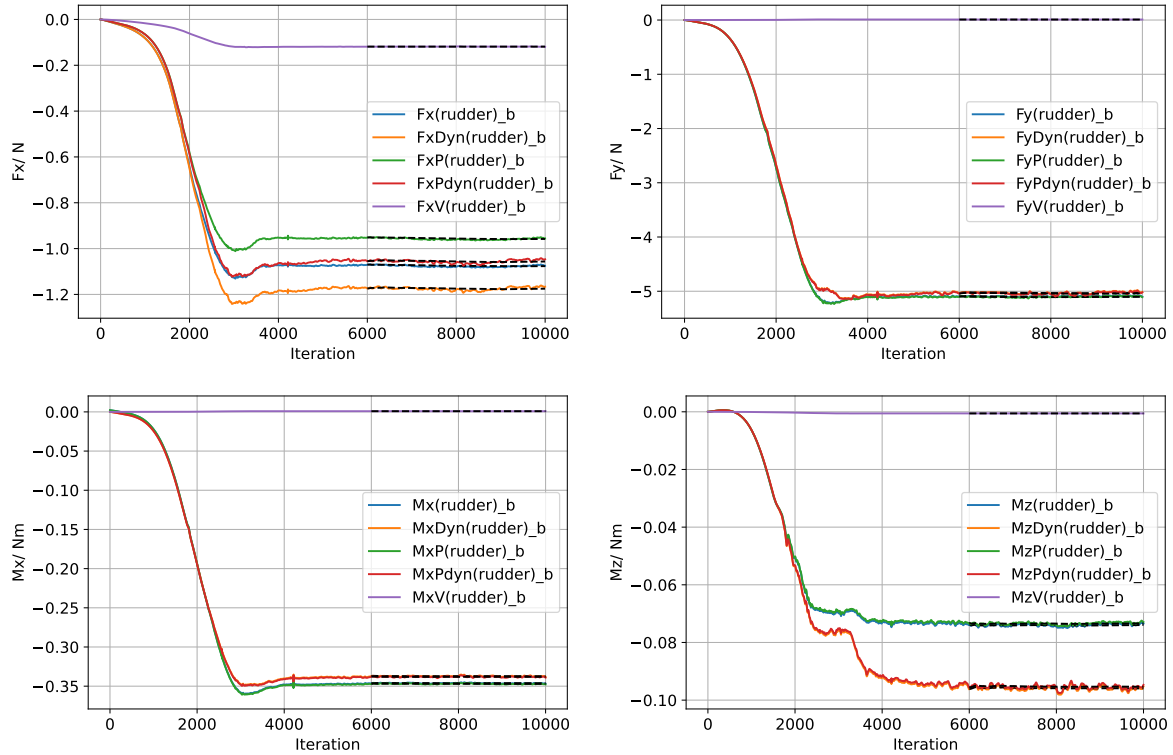
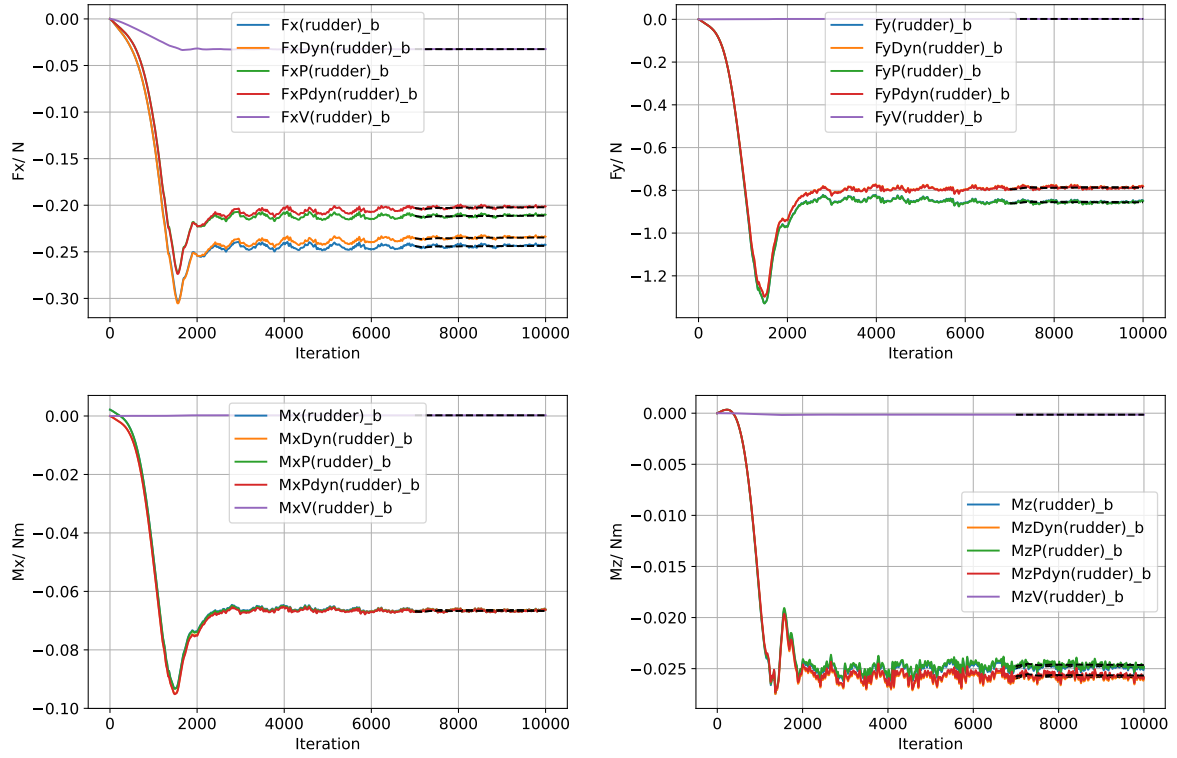
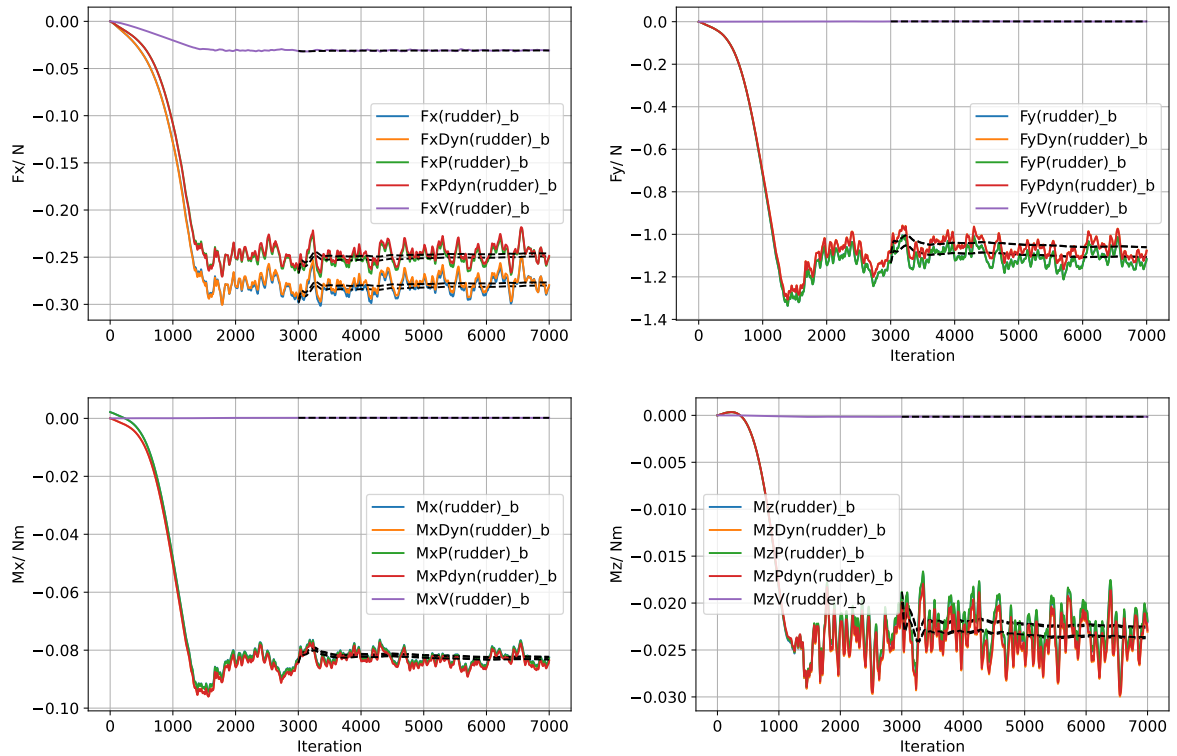


Figure 22 – Convergence of forces and moments acting on the rudder for $V = 1.0$ m/s and $\beta = 10^\circ$ assuming fully turbulent flow.

Figure 23 – Convergence of the forces and moments acting on the rudder at $V = 0.5 \text{ m/s}$ and $\beta = 10^\circ$ assuming fully turbulent flow.Figure 24 – Convergence of the forces and moments acting on the rudder at $V = 0.5 \text{ m/s}$ and $\beta = 10^\circ$ assuming laminar flow.

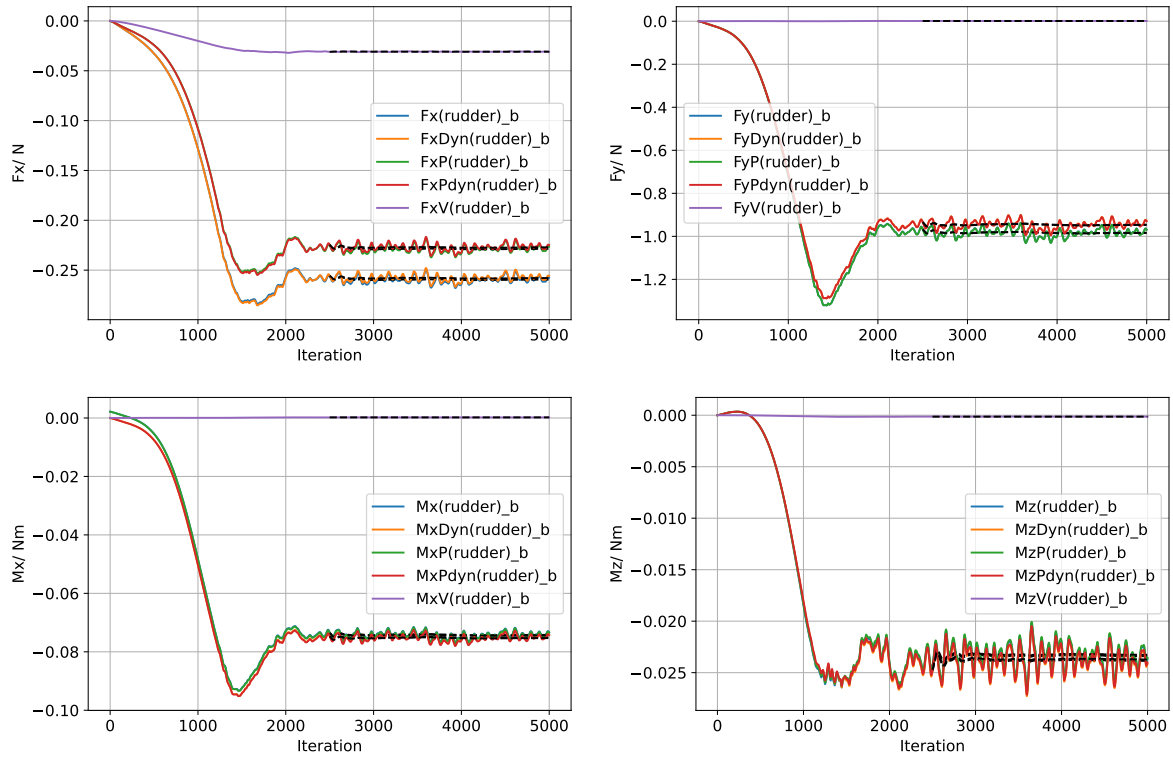


Figure 25 – Convergence of the forces and moments acting on the rudder at $V = 0.5$ m/s and $\beta = 10^\circ$ assuming free transition from laminar to turbulent flow.

4.3 Comparison with experimental results

4.3.1 Forces

The dimensionless experimental results for $\beta = 10^\circ$ (drag force C_X , lift/lateral force C_Y and yawing moment C_M) are shown in Fig. 26 together with the values obtained with CFD. Overall, the trends for the lift and drag show very similar behaviour: both the numerical and experimental results predict a local maximum for the lift and drag at $V = 0.8$ m/s and a local minimum for these quantities at $V = 0.5$ m/s. For high tow speeds ($V \geq 1.1$ m/s), the numerical lift results obtained using the turbulent flow assumption overlap with the experiments. For lower velocities, these results start to deviate from the experimental results, although similar trends are predicted. For the drag, the turbulent CFD results predict the same trend (with a constant offset) as the experiments for $V \geq 0.9$ m/s.

At low speed (e.g. $V = 0.4$ m/s), the lift predicted by the laminar computation is significantly higher (and closer to the experimental result) than the turbulent prediction. The distribution of pressure on both sides of the rudder for both cases is shown in Fig. 29. On the pressure side (Fig. 29a), the use of a turbulence model increases the area halfway the rudder with low pressure. On the suction side (Fig. 29b), the laminar cases generates a larger area near the leading edge (left rudder side) with a low pressure that provides lift. A cut plane at $z = -0.05$ m (at the position of the pressure holes) shows the pressure distribution around the rudder (Fig. 30), confirming the observation that for this condition, laminar flow will generate more lift.

At the lowest speeds, it appears that the numerical results fail to predict the experimental trends. It should be noted that the measured dimensional values are very small at low speeds and small differences can thus be blow up. When the dimensional values are compared (see Fig. 27), the numerical results at low speeds practically overlap with the measurements. Nevertheless, a visualisation of a horizontal cut through the flow field for the turbulent flow results at $V = 0.2$ m/s does show that for this case, the boundary layer detaches

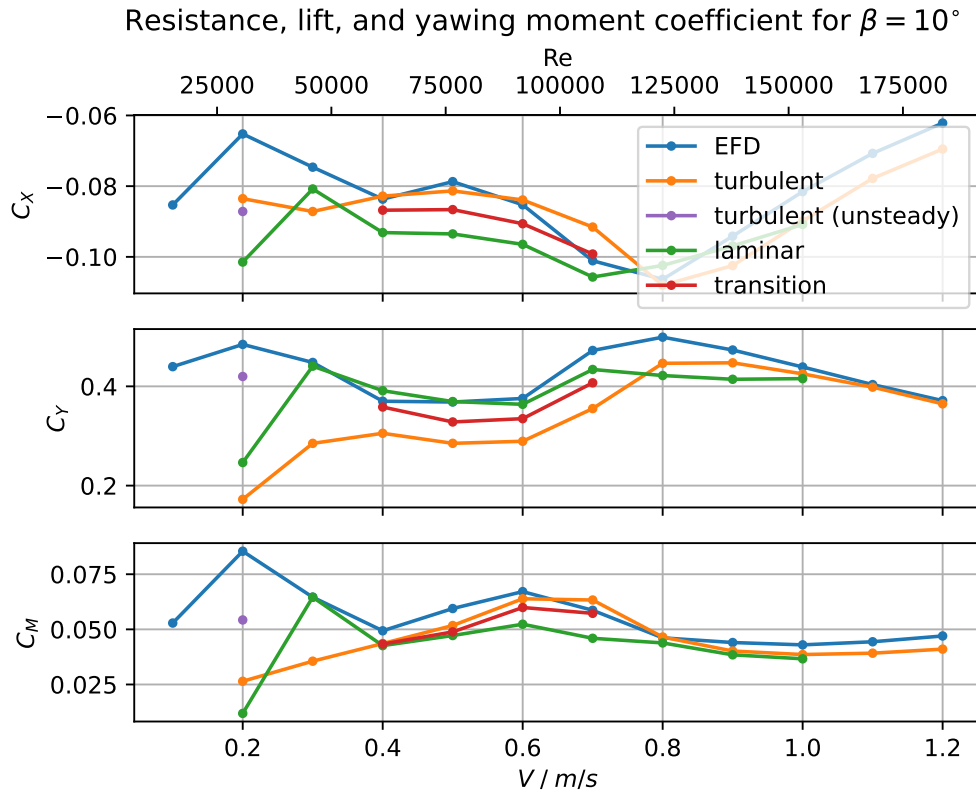


Figure 26 – Comparison of experimental and numerical values of lift, drag and yawing moment coefficients for drift angle $\beta = 10^\circ$.

from the rudder with (unsteady) flow separation as a consequence. Rerunning the computation in unsteady mode results in a significant difference in the velocity field in the plane $z = -0.5$ m, as shown in Fig. 28. The unsteady result for this case is also added to Fig. 26. For this particular case, both the resulting lift and yawing moment predictions are improved significantly, while the drag prediction is similar.

For velocities below $V = 1.0$ m/s, it is expected that transition from laminar to turbulent flow affects the results. This is clear from the numerical lift predictions using the laminar flow condition: these results are closer to the experimental values than the numerical results assuming fully turbulent flow (where a significantly lower lift value is predicted). For the three force components investigated, the results using the transition model fall in between the fully turbulent and fully laminar cases.

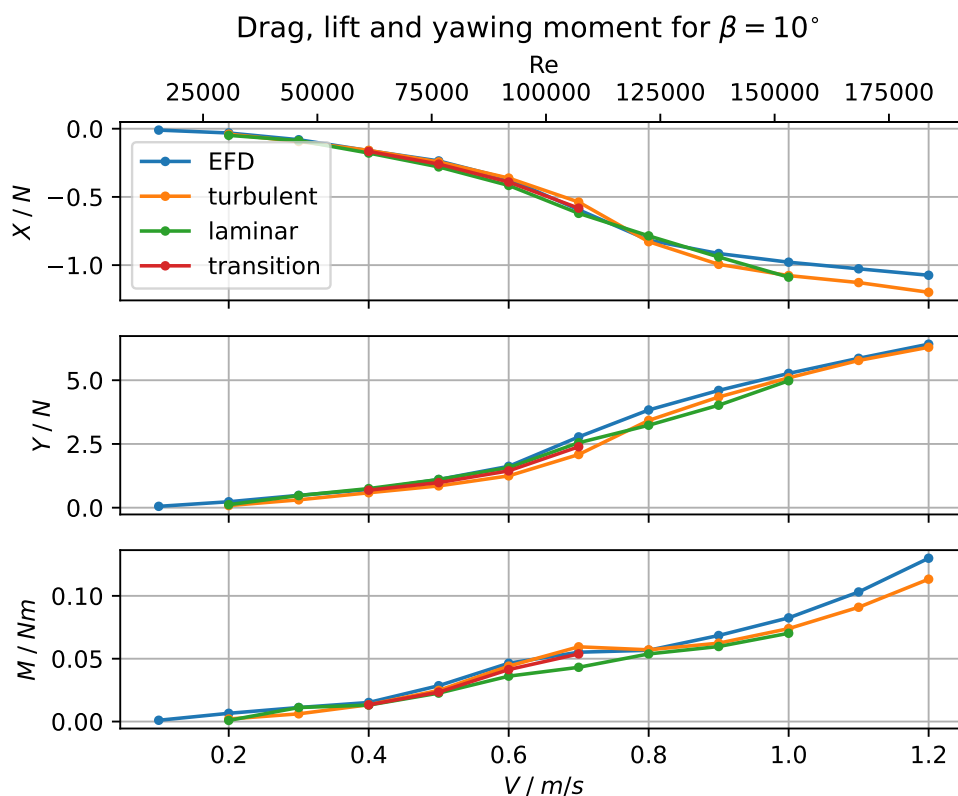


Figure 27 – Comparison of experimental and numerical values of lift, drag and yawing moment coefficients for drift angle $\beta = 10^\circ$.

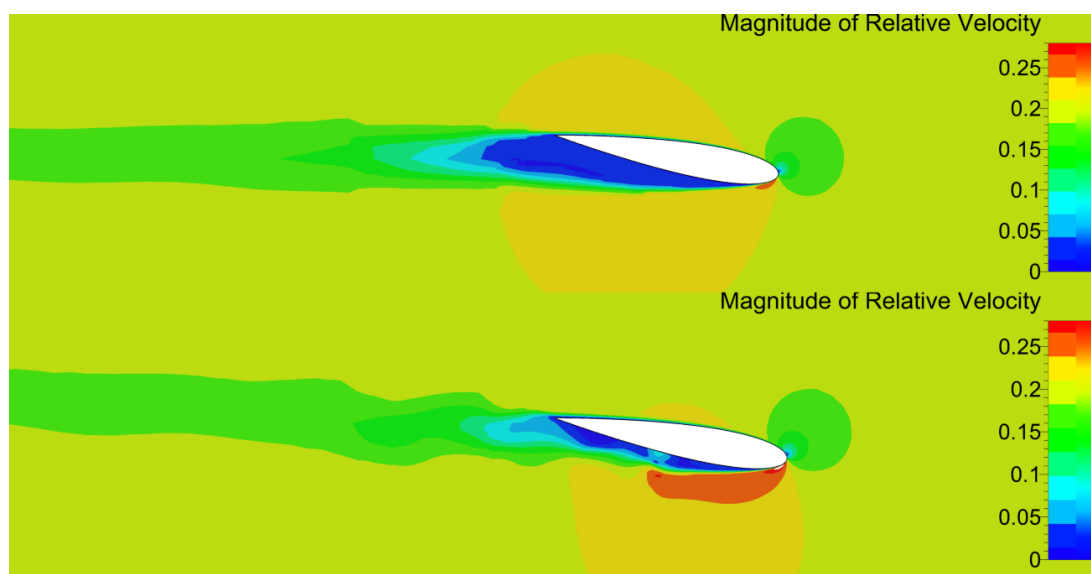


Figure 28 – Comparison of velocity field at $z = -0.05$ m for steady (top) and unsteady (bottom) turbulent flow assumption for drift angle $\beta = 10^\circ$ and $V = 0.2$ m/s.

4.3.2 Pressure measurements

The hydrodynamic pressure values measured at the four probes located in the face of the rudder are compared in Fig. 31 with values from the CFD computations (using the laminar, turbulent and transition assumptions for the turbulence model).

The trends as measured in the experiments are replicated in the numerical results using the turbulence model,

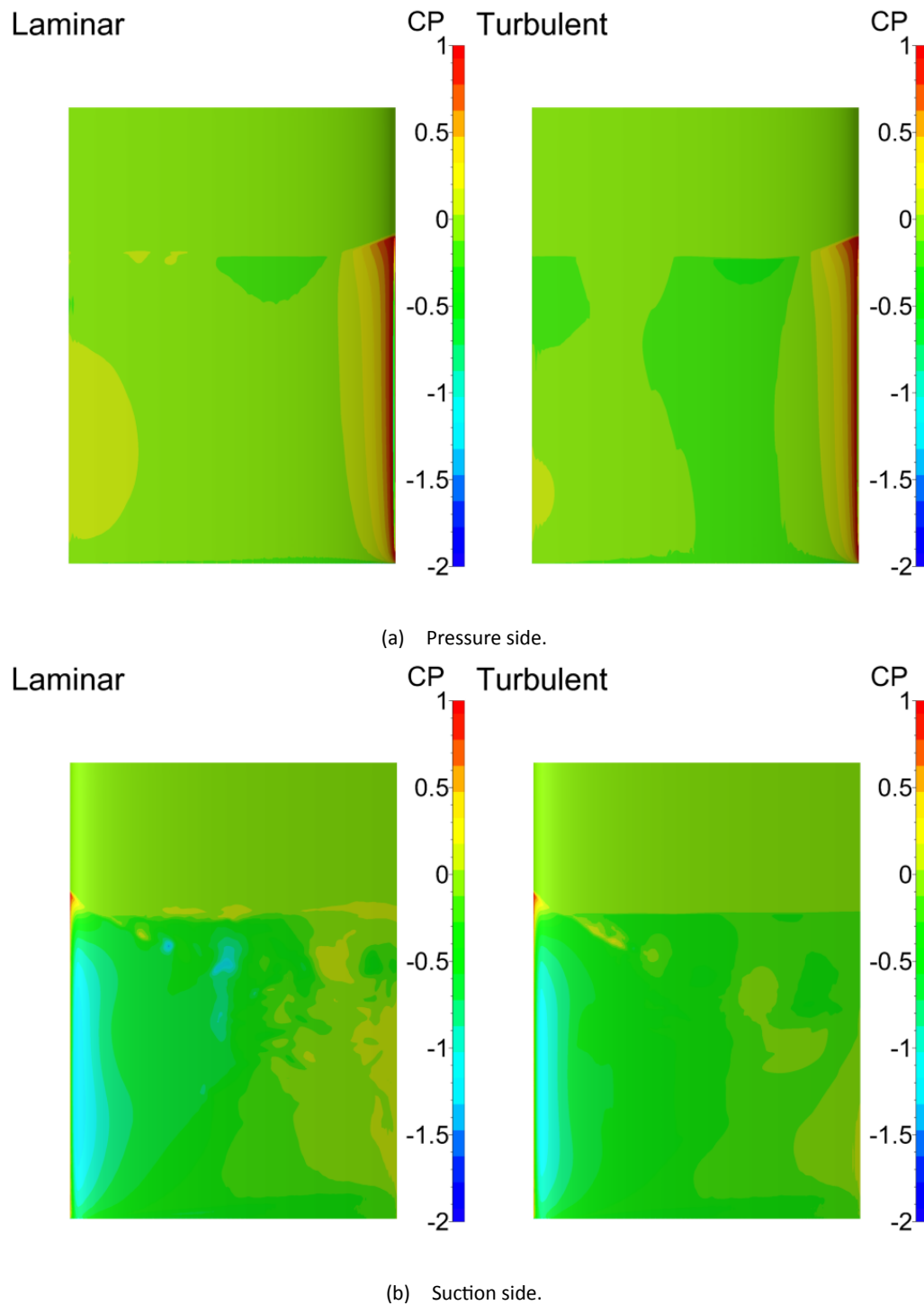


Figure 29 – Comparison of the pressure distribution on the rudder for the laminar and turbulent case at $V = 0.4 \text{ m/s}$ and $\beta = 10^\circ$.

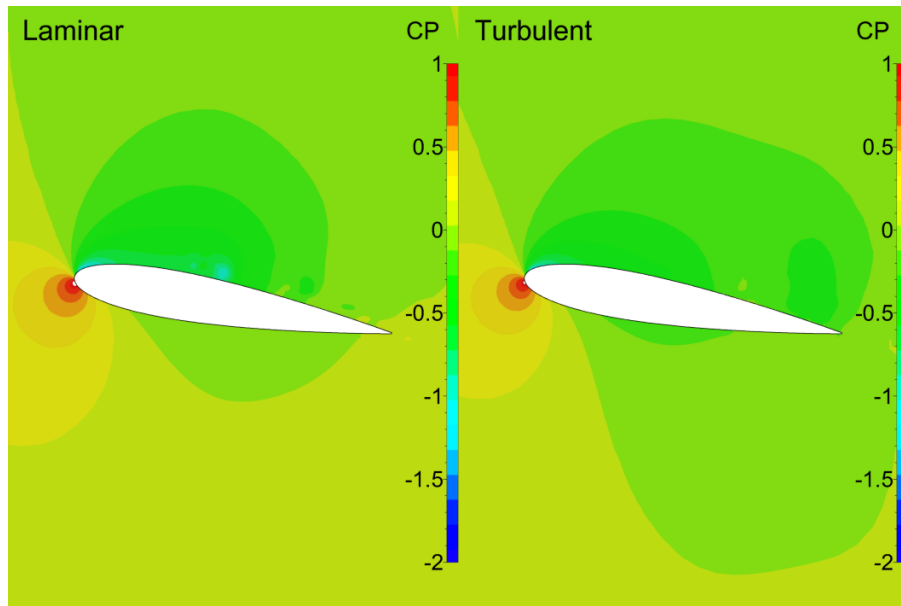


Figure 30 – Comparison of the pressure distribution in the plane $z = -0.05$ m for the laminar and turbulent case at $V = 0.4$ m/s and $\beta = 10^\circ$.

although the differences on an absolute scale are rather large for probe P4 (located closest to the leading edge, see Fig. 5). Initially, no computations were executed at $V = 0.6$ m/s, but given the local maximum for the pressure at probes P1 and P3 at that velocity, an extra computation was configured to verify that the numerical results predict the peak at the same speed. An additional computation at this speed is required to determine if the peak value as observed for probe P1 and P3, is present in the numerical results as well. At the highest speed, the discrepancy between

The laminar flow assumption does improve the pressure predictions at probes P2 and P4 for low velocities, but its correspondence is worse at the other two probes. As was the case for the force comparison, the results using the transition model fall on or in between the laminar and turbulent results. It should be noted that in order to measure the pressure on the rudder surface, circular holes with a diameter of 4 mm have been included in the rudder design. Results displayed in Fig. 31 were obtained at the centre of these holes. In areas with large gradients in the pressure field (e.g. for P2 and P3), the resulting pressure values will be very sensitive to the positions.

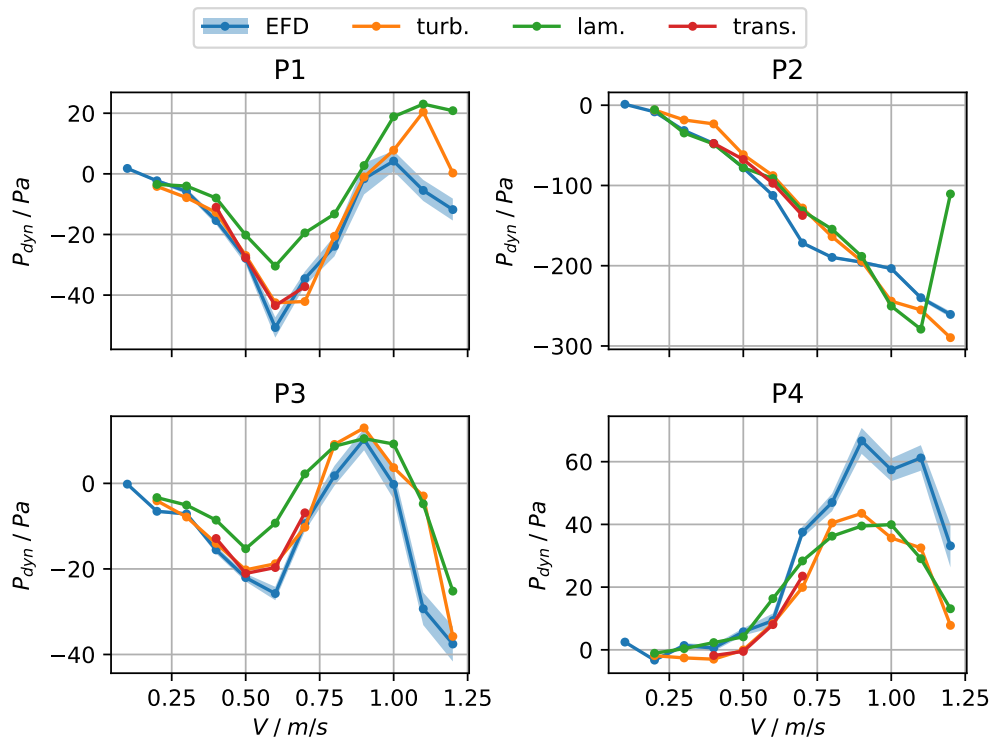


Figure 31 – Comparison of numerical and experimental hydrodynamic pressure values at the rudder probes.

5 Conclusions

The comparison between the experimental results and numerical results is encouraging: both the force comparison and the pressure probe comparison show that the CFD results are able to predict the trends as measured in the experiments. There are however differences, some of which can be attributed to the flow regime that is assumed in the computations (laminar, turbulent or natural transition). For low velocities, the assumption of fully turbulent (steady) flow breaks down, and a more advanced method that can model the transition from laminar to turbulent flow may be required. If this is not available, only the tests executed at the highest speeds should be used for validation purposes.

Given that only a single grid was used for all results (for which no grid convergence study was executed – due to the preliminary nature of the study), it is not extremely surprising that differences remain. Furthermore, the flow visualisations at the lowest speed have shown that the flow over the suction side of the rudder does not remain attached. For these cases, a second-order time integration scheme improves the results. Encouraging results have been obtained using the transition model. The availability of point pressure measurements on the rudder surface in addition to integral quantities (total forces and moments acting on the rudder) is a valuable addition when comparing CFD and Experimental Fluid Dynamics (EFD) results.

6 Acknowledgements

The experiments were conducted as part of the FWO project G0D5319N *CFD nautical bottom*.

References

- Brouwer, J.; Tukker, J.; Klinkenberg, Y.; Rijsbergen, M. van** (2019). Random uncertainty of statistical moments in testing: Mean. *Ocean Engineering* 182: 563–576 pp. DOI: 10.1016/j.oceaneng.2019.04.068
- Doddugollu, S. P.** (2024). Development of a CFD Model to Study Ship-fluid Mud Interaction. (PhD Thesis). KU Leuven: Faculty of Engineering Science: Leuven
- Sotelo, M. S.; Boucetta, D.; Van Hoydonck, W.; Delefortrie, G.** (2024). Numerical Study of the Hydrodynamic Forces Acting on a Surface-Piercing Hydrofoil in Natural Mud. *in: Proceedings of the 35th Symposium on Naval Hydrodynamics*. 35th Symposium on Naval Hydrodynamics. Nantes, France
- Sotelo, M. S.** (2024). Experimental Study and Numerical Simulations of Semi-Submerged Bodies Towed through Natural Mud Environments. (PhD Thesis). Ghent University: Faculty of Engineering and Architecture. ISBN: 9789463558518
- Van Hoydonck, W.; Delefortrie, G.; De Maerschallck, B.; Vantorre, M.; Mostaert, F.** (2017). Analysis of open-water rudder tests. Version 4_0. *FHR Report*, 00_057_5. Flanders Hydraulics Research: Antwerp, Belgium

DEPARTMENT **MOBILITY & PUBLIC WORKS**
Flanders Hydraulics

Berchemlei 115, 2140 Antwerp

T +32 (0)3 224 60 35

F +32 (0)3 224 60 36

waterbouwkundiglabo@vlaanderen.be

www.flandershydraulics.be